COMPUTER METHODS IN BIOMECHANICS AND BIOMEDICAL ENGINEERING, 2017
VOL. 20, NO. 1, 59–74
http://dx.doi.org/10.1080/10255842.2016.1198784

Taylor & Francis
Taylor & Francis Group

Computational model of mesenchymal migration in 3D under chemotaxis

F. O. Ribeiro[a,b], M. J. Gómez-Benito[b], J. Folgado[a], P. R. Fernandes[a] and J. M. García-Aznar[b]

[a]IDMEC, Instituto Superior Técnico, Universidade de Lisboa, Lisbon, Portugal; [b]Multiscale in Mechanical and Biological Engineering (M2BE), Aragón Institute of Engineering Research (I3A), Department of Mechanical Engineering, Universidad de Zaragoza, Zaragoza, Spain

ABSTRACT

Cell chemotaxis is an important characteristic of cellular migration, which takes part in crucial aspects of life and development. In this work, we propose a novel *in silico* model of mesenchymal 3D migration with competing protrusions under a chemotactic gradient. Based on recent experimental observations, we identify three main stages that can regulate mesenchymal chemotaxis: chemosensing, dendritic protrusion dynamics and cell–matrix interactions. Therefore, each of these features is considered as a different module of the main regulatory computational algorithm. The numerical model was particularized for the case of fibroblast chemotaxis under a PDGF-bb gradient. Fibroblasts migration was simulated embedded in two different 3D matrices – collagen and fibrin – and under several PDGF-bb concentrations. Validation of the model results was provided through qualitative and quantitative comparison with *in vitro* studies. Our numerical predictions of cell trajectories and speeds were within the measured *in vitro* ranges in both collagen and fibrin matrices. Although in fibrin, the migration speed of fibroblasts is very low, because fibrin is a stiffer and more entangling matrix. Testing PDGF-bb concentrations, we noticed that an increment of this factor produces a speed increment. At 1 ng mL^{-1} a speed peak is reached after which the migration speed diminishes again. Moreover, we observed that fibrin exerts a dampening behavior on migration, significantly affecting the migration efficiency.

ARTICLE HISTORY
Received 5 January 2016
Accepted 3 June 2016

KEYWORDS
3D mesenchymal migration; fibroblast; chemotaxis; platelet derived growth factor; phosphoinositide 3-kinase; Gillespie's algorithm

Introduction

Cell migration is a fundamental part of cell behavior and plays a central role in many aspects of life and biology, spanning from embryogenesis (Martin & Parkhurst 2004), immune response (Bogle & Dunbar 2010), angiogenesis (Geris et al. 2008) and wound healing (Shaw & Martin 2009; Valero et al. 2014), to the development of disease such as cancer and metastasis formation (Condeelis et al. 2005). Thus, it is really important to understand the mechanics of cell migration, given the variety of scenarios in which cells have to deploy their migratory skills. The process is coordinated by a complex set of internal and external factors such as temperature (Higazi et al. 1996), adhesion sites in the extracellular matrix (ECM) (Cukierman et al. 2001), ECM mechanical properties (Lo et al. 2000) and the gradient of chemical factors (Devrotes & Janetopoulos 2003; Cao et al. 2004; Roca-Cusachs et al. 2013). These latter chemo-attractants are responsible for chemotaxis, a phenomenon where cell movement is typically biased towards the chemo-attractant source.

In general, cell migration can be seen as a complex multi-physics and multi-scale problem that integrates biochemical reaction kinetics, cell-ECM interactions, and cell mechanics (Rangarajan & Zaman 2008; Kim et al. 2013). Actually, during chemotaxis, the biochemical interaction between a chemo-attractant factor and cell surface receptors triggers a cascade of internal signaling that provides a chemo-sensing mechanism. In response to that signaling cascade, cells increase their protrusions while attaching and pulling their surrounding ECM, thus generating a gradual advance. Depending on the cell type, different cell dynamics are observed which utterly determine their migration efficiency (Evan-Ram & Yamada 2005).

Actually, two distinct migration phenotypes for individual cells are described in the literature: amoeboid migration and mesenchymal migration (Friedl & Wolf 2010; Insall 2010; Swaney et al. 2010; Bear & Haugh 2014). The amoeboid migration mode, also called fast-migration, is observed in cells such as *Dictyostelium discoideum*, neutrophils and T cells (Lämmermann et al. 2008; Swaney et al. 2010; Beauchemin et al. 2007). This migration mode

CONTACT J. M. García-Aznar jmgaraz@unizar.es
The supplementary material for this paper is available online at http://dx.doi.org/10.1080/10255842.2016.1198784.

is characterized by a clear cell polarization, with a directional protrusion of pseudopods and lamillopodia across the cell front, which adhere to the ECM through focal adhesions (Borau et al. 2011). Actin-myosin complexes then contract and make the cell squeeze itself through the matrix, forcing cell progression through the ECM.

Conversely, mesenchymal migration, also called slow-migration, can be observed in mesenchymal stem cells (MSCs), fibroblasts (Deuel et al. 1991; Veevers-Lowe et al. 2011) and tumor cells (Giri et al. 2013). During mesenchymal migration the migration mechanism is quite different, because cells do not present a clear polarization as in the previous case (Petri et al. 2009). Instead, multiple competing protrusions emerge in different directions (Fraley et al. 2010; Moreno-Arotzena et al. 2014), adhere through focal adhesions which are tractioned when longitudinal stress fibers contract (Even-Ram et al. 2007; Vicente-Manzanares et al. 2011). This 'tug-of-war' behavior creates a less efficient locomotion of the cell (Friedl & Wolf 2009).

Fibroblasts and MSCs directional migration is mediated by the chemosensing of their surroundings through different membrane receptors. One known mechanism is the one that involves the tyrosine kinase class receptors (RTKs) (Pelletier & Boyten 1994; Poukkula et al. 2011). After reacting with the ligand the activated form of the receptor mediates the recruitment and activation of phosphoinositide 3-kinase (PI3K). PI3K is at the center of the migration signaling hub as it promotes the WAVE regulatory complex that in turn activates the Arp2/3 complex (Lebensohn & Kirschner 2009). This chain of events leads to the formation of new adhesions, promotes a further stabilization of protrusions and enhances the polymerization of actin. The myosin II, present in cells, will bind to the bundled actin stress fibers, ultimately producing cell protrusion contraction (Campellone & Welch 2010; Rotty et al. 2013).

The premise of this work is to provide a better understanding on three-dimensional (3D) mesenchymal migration during chemotaxis. In particular, we aim to study how different chemo-attractant gradients and ECMs, affect cellular speed and migration efficacy during 3D chemotaxis.

Therefore, here we propose a novel *in silico* 3D model to simulate mesenchymal 3D migration on various types of fibrous matrices and under different chemical concentrations. Therefore, following the previous multi-physics and multi-scale characteristics, we propose the following strategy: (1) first we emulate the initial segment of the signaling cascade triggered by receptor activation; (2) then we simulate protrusions occurrence, growth and retraction which interact with the ECM; (3) finally cell motion follows protrusion contraction. The results found *in silico* – speeds, trajectory and persistence – are then quantitatively compared with *in vitro* studies of human fibroblasts under a PDGF-bb (platelet-derived growth factor –bb) chemotactic gradient (Moreno-Arotzena et al. 2015).

Materials and methods

Mechanical cell model

The 3D structure of the cell is geometrically modeled (Figure 1(A)) as a set of bars in 3D, representing the three dimensional dendritic protrusions diverging from a central connecting point that represents the cell body (Figure 1(B)). This central connecting point mostly exists for modeling purposes as the point where all the bars are connected, it can be associated to the cell nucleus or alternatively to the cell centrosome.

The model is based on the *in vitro* observation of migrating fibroblasts, where we can identify three main stages: first the chemosensing of the chemo-attractant factor, then the extension of dendritic protrusions and finally their contraction leading to cell progression.

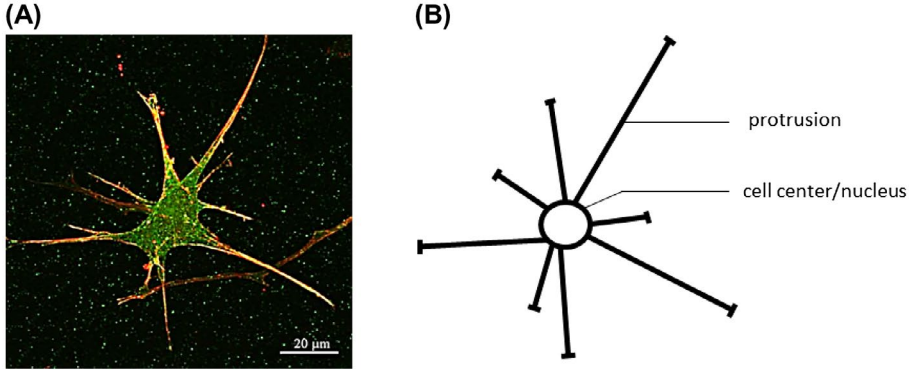

Figure 1. (A) Image of a migrating fibroblast under a PDGF-bb gradient (taken from Moreno-Arotzena et al. 2015). (B) Simplified 3D scheme used to represent the fibroblast shown on the left.
Note: Briefly, the cell is defined as a set of bars, representing the protrusions, united around a central body, representing the cell nucleus.

Chemosensing model

During chemosensing cells probe the chemical cues on their surrounding micro-environment. Indeed the many receptors on the cell membrane surface react with specific chemo-attractant factors (Devrotes & Janetopoulos 2003; Cao et al. 2004; Roca-Cusachs et al. 2013; Moreno-Arotzena et al. 2015) and, by mean of those chemical reactions occurring on the membrane surface the cell is able to sense its surroundings. For the purpose of modelling this chemosensing phenomenon occurring on the membrane, we represent the cell membrane as a spherical surface with a radius of 70 μm, centered around the center point of the mechanical cell model. This size has been determined from images of human fibroblasts embedded in 3D collagen- and fibrin-based matrices (Moreno-Arotzena et al. 2015).

Biochemically, as we can observe in Figure 2(A), chemosensing starts with the reaction between the chemo-attractant factor and their specific receptors on the cell membrane. Switched on, the receptors activate other molecules in the cytosol that propagate internally the signal received at the membrane level. The triggering of the signaling cascade can ultimately regulate protrusion growth and retraction.

In this work, we consider the 3D migration of fibroblasts under chemotactic conditions. For the purpose of simulating chemosensing, we considered the simplified set of reactions that occurs at the cell membrane level, as represented in Figure 2(B).

For this reaction model, we assume that one chemo-attractant molecule *F* binds to one *RTK* receptor which is then, while switched on, able to turn the cytosolic messenger *PI3K* into its activated form $PI3K^*$(Hatakeyama et al. 2003; Hawkins et al. 2006). Although several other messengers are involved during chemotaxis, our study does not go beyond *PI3K* activation. In fact, Weiger et al. (2010) showed that *PI3K* activation and cytosolic gradients are closely related with migration direction and protrusion growth and stabilization. From a time perspective only, the scheme in Figure 2 can be fully described by a set of ordinary differential Equations in (1), where each equation denotes the variation rate of each chemical species

$$\begin{cases} \frac{\partial RTK}{\partial t} = -k_1 RTK \cdot [F] + k_{-1} RTKF \\ \frac{\partial RTKF}{\partial t} = k_1 RTK \cdot [F] - k_{-1} RTKF \\ \frac{\partial PI3K^*}{\partial t} = k_2 RTKF \cdot PI3K - k_3 PI3K^* \\ \frac{\partial PI3K}{\partial t} = -k_2 RTKF \cdot PI3K + k_3 PI3K^* \end{cases} \quad (1)$$

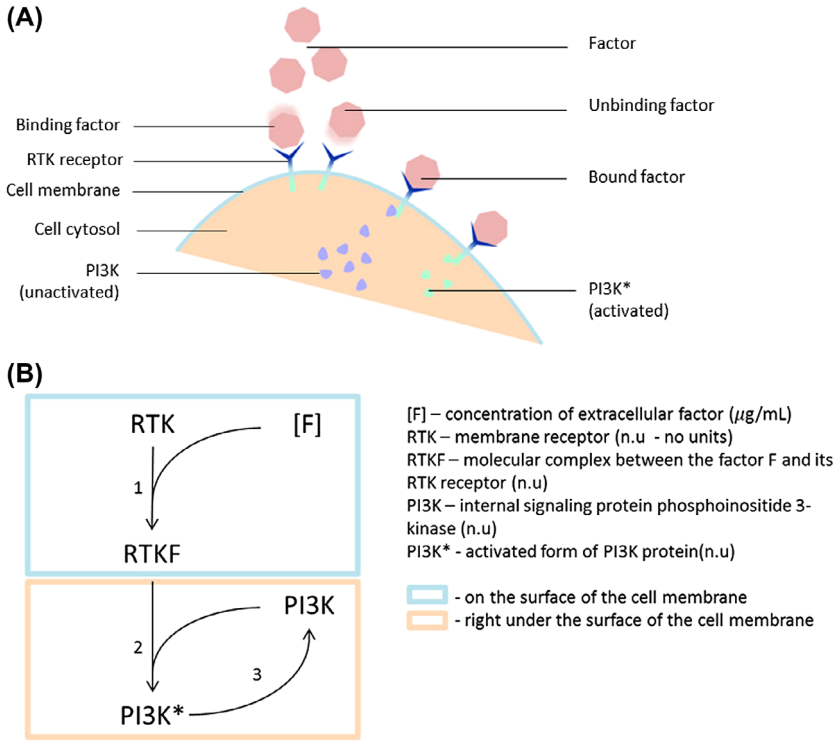

Figure 2. (A) Scheme of a cell membrane. The cross-membrane RTK receptors bind to the factor present in the cell surroundings. Later on, the RTK-factor complexes catalyze the activation of the PI3K in the cytosol. This transduction passes the information from the outer media into the cell. (B) Schematic representation of the set of reactions that take place next to the membrane.
Notes: 1 –represents the forward and reverse reactions that occur between the factor and the receptor. 2 –represents the activation of PI3K in the cytosol. 3 –represents the natural deactivation of PI3K.

where k_i is reaction i forward rate and k_{-i} is reaction i reverse rate. Assuming chemical reactions are stochastic processes well described by a Poisson distribution (Ueda & Shibata 2007), the evolution of this system was computed via Gillespie's algorithm (Gillespie 1976; Higham 2007). Gillespie's algorithm is a numerical method used to efficiently emulate the evolution of chemically reactive systems; it predicts the system equilibrium while preserving the randomness of the chemical reactions involved.

So far, we explored chemosensing from a temporal perspective. However, gradient sensing presumes the detection of the gradient spatial orientation. The reaction between factor *F* and its *RTK* receptor (reaction 1) is spread across the whole cell membrane. Assuming that membrane receptors are homogenously distributed over the cell surface, the density of activated receptors would only depend on the distribution of factor *F* on the cell surface (see, for example, Figure 5(B) to show the distribution of the factor on the cell surface, mapping this spherical distribution onto a flat surface). In fact, there will be more activated receptors where the concentration *F* is greater and there will be less activated receptors where the amount of *F* is lower (Ueda & Shibata 2007). In this way cells can sense the gradient spatial orientation.

Mathematically, and maintaining the assumption that chemical reactions are well approximated by a random Poisson's process, the receptor activation over a domain with varying concentration of factor *F* can be thought as a multivariate non-homogenous Poisson's distribution, which we solved using the Inverse Method described by Saltzman et al. (2012).

Therefore, we assume that each activated receptor can lead to the generation of *PI3K** which, according to Weiger et al. (2010), stabilizes protrusion extension and growth. Importantly, the amount of *PI3K** molecules varies spatially across the cell surface, but also in time following the system in (1). Thus, to help to determine the tempo-spatial variation we defined the variable $s(\alpha, \beta, t)$ which gathers the information of the spatial persistence of *PI3K** activation across time *t*, in a space location of the cell surface defined by the coordinates (α, β) (since we consider a 3D model of a cell, the cell membrane can be represented by a flat surface defined by the pair polar coordinates α and β).

First, at a fixed instant of time *t*, the spatial persistence of *PI3K** can be captured by performing a 2D convolution over the cell surface, as represented in Equations (2) and (3):

$$s_t(\alpha, \beta) = d_{PI3K^*}(\alpha, \beta) * p(\alpha, \beta) \tag{2}$$

$$s_t(\alpha, \beta) = \int_{-\infty}^{+\infty}\int_{-\infty}^{+\infty} d_{PI3K^*}(u, v)p(\alpha - u, \beta - v)\mathrm{d}u\mathrm{d}v \tag{3}$$

Here the convolution is defined between $-\infty$ and $+\infty$ and with the dummy variable *u* and *v* as per definition. Here $s_t(\alpha, \beta)$ represents the amount of activated *PI3K** across the cell membrane surface at a time *t*. That signal is measured according to the convolution between $d_{PI3K^*}(\alpha, \beta)$ – the distribution of *PI3K** molecules across the membrane – and $p(\alpha, \beta)$ a convolution windows roughly the size of a protrusion. As a first approach, the window size for the protrusion was defined as a circular window of 10° (degrees) in diameter.

With this definition we now know where *PI3K** is preferably activated. Yet, how this signal is accumulated through time is also important because cell migration is a time dependent event. To detect where *PI3K** molecules persist throughout the time cells migrate, the signal $s_t(\alpha, \beta)$ was sampled at a frequency of 1 Hz and $s(\alpha, \beta, t)$ – the cumulative signal – was defined as

$$s(\alpha, \beta, t) = \sum_{t=t_0}^{t_f} s_t(\alpha, \beta) \tag{4}$$

where $s_t(\alpha, \beta)$ represents again the amount of activated *PI3K** across the cell membrane surface at a time *t*, t_0 and $t_f = t$ define the time period through which the 1 Hz sampling is evaluated and $s(\alpha, \beta, t)$ is the cumulative signal of *PI3K**. For practical reasons, from now on $s(\alpha, \beta, t)$ will be denoted by just *s*.

As we will see in the next section, the persistence of this signal is used to determine the spots where protrusions are more likely to appear. The birth rate of this protrusion is roughly 0.002 Hz as measured *in vivo* by Weiger et al. (2010), and because this happens at such a low rate, sampling the signal at 1 Hz was deemed adequate (according to signal sampling standards) as the sampling frequency is higher than the corresponding to the protrusion formation rate.

Hence, with the methods described above, we can compute the signal of *PI3K** generated across the cell membrane. In particular, any measured peak of signal *s* would reflect the spatio-temporal persistence of *PI3K** and thus, this variable will define a likely spot for protrusion to appear.

Modeling protrusion dynamics

To describe protrusion dynamics, we consider that each protrusion can be represented as a vector. Hence, we denote protrusion *i* as the vector $\boldsymbol{f}^i$, which can be vectorially defined as

$$\boldsymbol{f}^i = \|\boldsymbol{f}^i\|\boldsymbol{e}_i \tag{5}$$

where $||\boldsymbol{f}^i||$ is the length of protrusion i and $\boldsymbol{e}_i$ is the unit vector of the protrusion longitudinal axis.

We consider that protrusion grows and stabilizes where the *PI3K** signal s is stronger (Weiger et al. 2010) and becomes smaller or disappears where the signal s is weaker. We assume that a new protrusion is stabilized and grows longitudinally whenever the detected signal s is above the threshold $s_{\text{new—protrusion}}$. Therefore, the onset of novel protrusions only occurs at locations of the cell surface where the chemical signal s is higher than $s_{\text{new—protrusion}}$. This follows the idea suggested by many authors that a minimal amount of signal should be obtained for cells to react and grow protrusion (Ueda & Shibata 2007; Weiger et al. 2010; Jilkine & Edelstein-Keshet 2011). Also, $s_{\text{new\_protrusion}}$, was estimated so as to obtain an average protrusion birth rate of roughly 20 min as measured *in vivo* by Weiger et al. (2010).

Once one dendritic protrusion has been formed, the dynamics of its length will depend on the level of the detected signal s. Thus, if the detected signal s is above the threshold s_{growth} it will reinforce any pre-existent protrusion and if it is lower than this threshold the protrusion will retract. Actually, if the signal s is below s_{ret} we consider that there is not enough signal remaining to keep protrusion growth and adhesion causing the protrusion to destabilize and ultimately resulting in retraction. Equation (6) summarizes dendritic protrusion (ε^P) or retraction (ε^R) behavior depending on cumulative signal strength s:

$$\varepsilon^P.\mathbf{e}_i = \begin{cases} \varepsilon_p^C.\mathbf{e}_i, & s_{\text{growth}} < s \\ 0, & s \le s_{\text{growth}} \end{cases} \qquad \varepsilon^R.\mathbf{e}_i = \begin{cases} \varepsilon_r^C.\mathbf{e}_i, & s \ge s_{\text{ret}} \\ -\mathbf{e}_i, & s < s_{\text{ret}} \end{cases} \tag{6}$$

where the scalar ε^P and ε^R define the longitudinal strain rate due to the dendritic protrusion or retraction.

To compute this longitudinal strain rate, we first have to know the strain field. The tensor $\boldsymbol{\varepsilon}_k^C$ corresponds to the constrained strain rate field ($k = p, r$; p protrusion and r retraction) and contemplates only the strain rate in the longitudinal direction $\varepsilon_k^C.\mathbf{e}_i$, thus being mathematically described as $\boldsymbol{\varepsilon}_k^C = \varepsilon_k^C.\,\mathbf{e}_i \otimes \mathbf{e}_i$.

Additionally, we also define the tensor $\boldsymbol{\varepsilon}_k^f$ for the stress free growth/retraction (it occurs only when there is not any ECM surrounding the protrusion). $\boldsymbol{\varepsilon}_k^f$ also contemplates strain only in the longitudinal direction and can be mathematically described as $\boldsymbol{\varepsilon}_k^f = \varepsilon_k^f.\,\mathbf{e}_i \otimes \mathbf{e}_i$. There, the scalar strain $\boldsymbol{\varepsilon}_k^f$ was defined as a function of the signal increment δ_s:

$$\varepsilon_k^f = \begin{cases} \dfrac{1}{\|\boldsymbol{f}^i\|}\dfrac{\alpha_{\text{gr}}\delta s}{(\beta_{\text{gr}}+\delta s)}, & \delta s \ge 0 \text{ (growth)} \\ \dfrac{1}{\|\boldsymbol{f}^i\|}\dfrac{\alpha_{\text{ret}}\delta s}{(\beta_{\text{ret}}+\delta s)}, & \delta s < 0 \text{ (retraction)} \end{cases} \tag{7}$$

α_{gr} and β_{gr} are two parameters that regulate protrusion growth, α_{ret} and β_{ret} are two parameters to model protrusion retraction, δ_s is the increment in signal s between two time instants. In fact, the mechanism that promotes cell motion through myosin contraction also provides a negative feedback to PI3K activation (as suggested by Weiger et al. 2010). Therefore, we assume that when a protrusion is retracted, some signal would be lost due to negative feedback. For the loss of signal due to retraction we consider a simple decay defined by parameter $\lambda = 0.21\ \text{min}^{-1}$ (Weiger et al. 2010). In fact, Weiger et al. (2010) measured *in vivo* that from birth to death, a protrusion would last 5 or 6 min. Therefore, to give the chance for the protrusion – and its signal – to vanish within that time frame, we considered half-life decay of 3.3 min, i.e. defined by a decay parameter = $0.21\ \text{min}^{-1}$. We also consider a time-dependent wear of protrusion signal, which wore out with time, following 30 min half-life decay (Weiger et al. 2010).

During dendritic protrusions, they push and exert forces on the ECM. Therefore, the mechanical properties of the ECM exert a regulatory role on the final extension or retraction of protrusion, restricting its growth or retraction, as was in fact suggested by Liou et al. (2014). To simulate this phenomenon, we consider a protrusion to be analogous to an elastic ellipsoid inclusion embedded in the ECM; from this perspective this ECM can be assumed as an infinite elastic body. Hence, the ECM restricts both growth and retraction and both protrusion and ECM are stressed. Actually, in 1957, Eshelby found the analytical solutions of ellipsoidal elastic inclusions in an infinite elastic body (Eshelby 1957; Clyne & Withers 1995). Therefore, we propose to make the analogy between cell protrusions with ellipsoid inclusions, modeling protrusion growth as the expansion of small ellipsoid inclusions inside a surrounding matrix. Therefore, we propose to follow the Eshelby's description of this phenomenon where the growth/retraction of protrusion is set to follow the relation

$$\tilde{\boldsymbol{\varepsilon}}_k^c = \mathbf{S}\left[\left(\mathbf{C}_I - \mathbf{C}_M\right)\mathbf{S} + \mathbf{C}_M\right]^{-1}\mathbf{C}_I\tilde{\boldsymbol{\varepsilon}}_k^f \tag{8}$$

where $\boldsymbol{C}_I$ is the elasticity tensor of the protrusion, $\boldsymbol{C}_M$ is the elasticity tensor of the surrounding ECM, $\boldsymbol{S}$ is the ellipsoid shape tensor, the vector $\tilde{\boldsymbol{\varepsilon}}_k^c$ represents protrusion growth or retraction while constrained by the ECM and the vector $\tilde{\boldsymbol{\varepsilon}}_k^f$ represents the protrusion stress free expansion or retraction (when no matrix restrict the deformation of the protrusion). Both $\tilde{\boldsymbol{\varepsilon}}_k^c$ and $\tilde{\boldsymbol{\varepsilon}}_k^f$ are in Voigt notation and represent the strain second-order tensor $\boldsymbol{\varepsilon}_k^C$ and $\boldsymbol{\varepsilon}_k^f$ respectively. For this approach, we have to consider a linear elastic behavior for the ECM, using as elastic constants the values indicated in Table 3.

Finally, we can update the protrusion length from one time step to another with Equation (9) for each dendritic protrusion, taking the value of ε from Equation (6):

$$\boldsymbol{f}^i_{n+1} = \left(\boldsymbol{\varepsilon}^P + \boldsymbol{\varepsilon}^R\right).\|\boldsymbol{f}^i_{\mathbf{n}}\|\mathbf{e}_i \tag{9}$$

Modelling cell body translocation

Each protrusion is considered to contract independently and, when contracting, they generate a traction force which reaction is sensed by the cell body, resulting in cell progression. As represented in Figure 3, the cell body will sense the corresponding reaction forces, which are countered by the drag generated by the strong adhesion with the surrounding ECM (Zaman et al. 2005; Borau et al. 2011; Kim et al. 2013).

Proceeding with the force equilibrium equation we write

$$\boldsymbol{F}_{drag} + \sum_{i=1}^{n} \boldsymbol{F}^i_R = 0 \tag{10}$$

where $\boldsymbol{F}_{\text{drag}}$ is the drag force exerted by the ECM on the cell body and $\boldsymbol{F}^i_R$ are the reaction forces supported by the cell body due to the retraction force of each protrusion i. The drag force can be simply defined as

$$\boldsymbol{F}_{\text{drag}} = 6\pi r\eta\mathbf{v} \tag{11}$$

where r is the cell radius, η is the ECM viscosity and $\boldsymbol{v}$ is the cell speed (see Table 3) (Paralkar et al. 1992; Borau et al. 2011).

As a simplification, we assume that a longer protrusion presents a larger adhesion surface, because there is a high probability that adhesion proteins may connect these thin protrusions with the ECM. Thus we suggest in Equation (12) a relationship between the contractile force magnitude (due to myosin heads sliding through the actin) and the protrusion length:

$$\boldsymbol{F}^i_{\text{trac}} = -\alpha_{\text{adh}}\boldsymbol{f}^i \tag{12}$$

where $\boldsymbol{F}^i_{\text{trac}}$ is the contractile force, α_{adh} is a constant that defines adhesion and $\boldsymbol{f}^i$ is the vector representing the protrusion. Note that as suggested in Figure 3, in this first approach the traction forces $\boldsymbol{F}^i_{\text{trac}}$ are assumed identical in magnitude to their corresponding reaction forces $\boldsymbol{F}^i_R$.

From experimental observations (Starke et al. 2013; Moreno-Arotzena et al. 2014), we remarked that the direction of each cell haul seems to be aligned with one of its protrusion. In fact, it is not difficult to assume that the protrusion with which cell motion is aligned is the one applying a higher contractile force. Based on this observation, we consider this assumption where one protrusion at the time effectively adheres, tractions and promote cell motion. Also, given the assumption taken for Equation (12), we consider that at each instant the longest protrusion would the one leading cell motion. This hypothesis is based on the experimental results observed in the work of Moreno-Arotzena, as can be clearly observed in the videos provided in this work (Moreno-Arotzena et al. 2014).

Therefore, in this work, we assume two different types of protrusions: adherent and non-adherent (Starke et al. 2013). In fact, we consider that while simply protruding and retracting, protrusions adhere to the ECM, causing it to deform according to their movement. However, during cell motion we assume that only the leading/longest protrusion remains adhered, whilst the others become non-adherent. So, in this way, the cell is able to drag all its protrusions while still migrating.

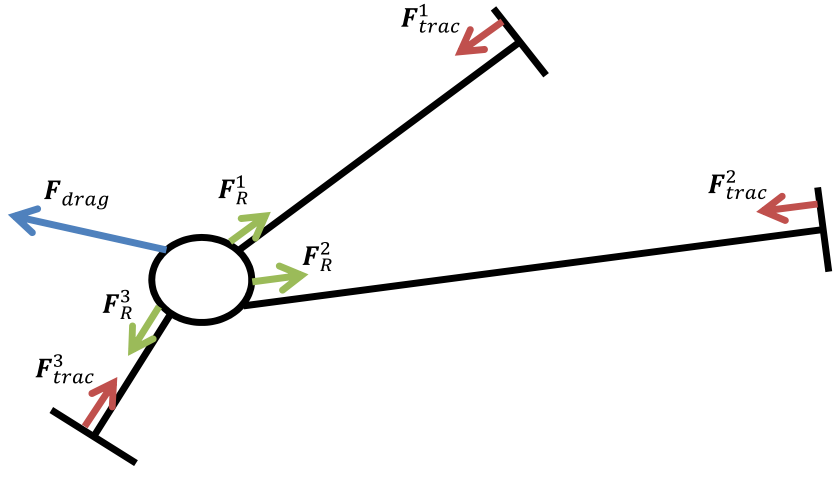

Figure 3. Schematic of the cell depicting the traction forces F^i_{trac}, reaction forces F^i_R and drag force $\boldsymbol{F}_{\text{drag}}$. The identity index i designates each filopodia.

Reorganizing these equations, we describe the set $\{\boldsymbol{f}^i\}$ as the ensemble of protrusion in one cell. Combining Equations (10)–(12) we can write the equation of motion for one cell

$$\begin{aligned} &\eta v - \alpha_{\text{adh}} \cdot \boldsymbol{f}^j = 0 \\ &\text{with } j = \max_i \{\|\boldsymbol{f}^i\|\} \end{aligned} \tag{13}$$

i.e. $\boldsymbol{f}^j$ is the longest protrusion. Basically this approach underlines the hypothesis the longest protrusion is the one with more adhesion and will thus lead the way.

Computational implementation

The three described mechanisms were numerically implemented in Python following the scheme shown in Figure 4. To start the simulation, we need an initial spatial distribution of the chemical factor that regulates cell response. In this work, we consider that an initial linear gradient of the PDGF-BB factor is distributed in the domain. With this concentration as initial stimulus, the chemosensing reaction equations are numerically solved by means of the Gillespie's algorithm. Hence, the chemosensing module provides information on the spatial distribution of the activated form of PI3K*, which will determine the preferential spatial directions for protrusion growth. We then apply the protrusion mechanical equilibrium Equation (10), and going from protrusion to retraction, each protrusion reaches its new length. All the mechanical equations are solved analytically by means of a computer-based algorithm.

Finally, and according to the motion Equation (13), we assume that the longest protrusion is the one that exerts most traction force, thus leading cell motion. This equation is solved explicitly, because from the forces that affect one cell, its speed is computed for each time increment.

Thus, we consider the factor F to the PDGF and its corresponding RTK receptor, called PDGF-R, which mediates PI3K activation. Both the initial amounts of each reactant and the reaction rates were obtained from the literature and are presented in Tables 1 and 2 respectively.

Also, each concentration case was simulated under the influence of two different ECMs – collagen and fibrin – (Moreno-Arotzena et al. 2015), whose properties are presented in Table 3.

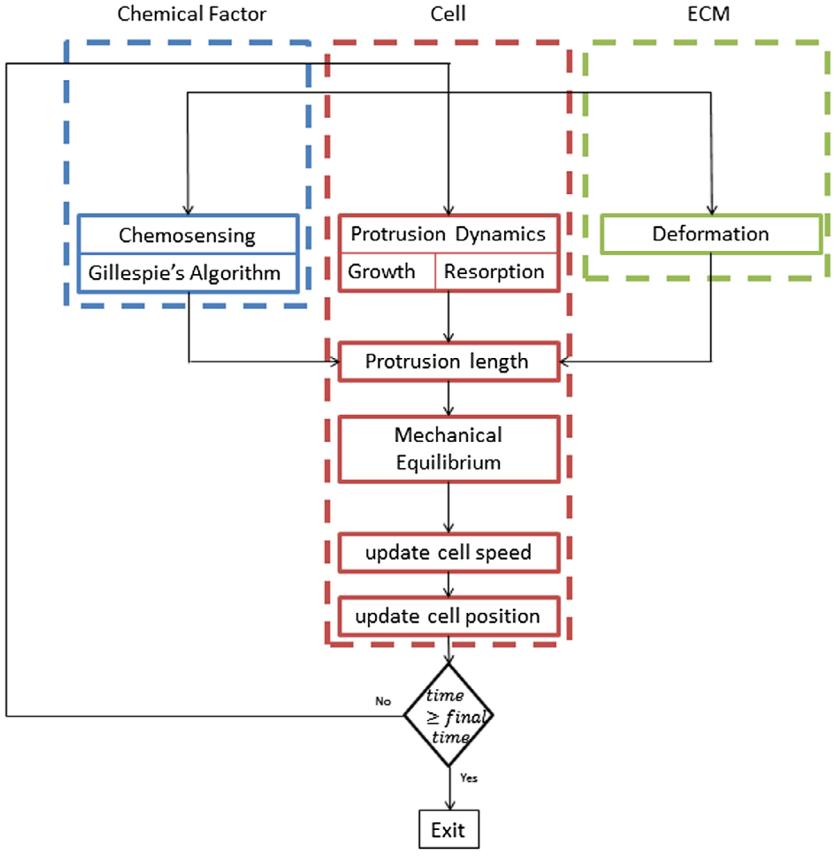

Figure 4. Scheme of the numerical algorithm used to simulate and regulate 3D cell migration under chemotaxis conditions.
Notes: Here we depict the three mechanisms that coordinate cell chemotaxis: chemosensing of the chemical factor, cell protrusion dynamics and the interaction between the cell and the ECM. Note that the stochastic aspect of cell migration is preserved mainly through the randomness of the chemosensing.

Table 1. Initial conditions.

Molecules	Amount
# PDGF-R	4275 (Paralkar et al. 1992; Miller et al. 2000)
# PI3K	75×10^3 (Hatakeyama et al. 2003)
# PI3K*	0

Table 2. Reaction constants for the activation pathway.

Reaction *i*	k_i	k_{-i}
1	$k_1 = 735\ nM^{-1}\ s^{-1}$ (Heinecke et al. 2009)	$k^{-1} = 0.01\ s^{-1}$ (Heinecke et al. 2009)
2	$k_2 = 0.0004\ s^{-1}$ (Hatakeyama et al. 2003)	N.A
3	$k_3 = 1\ s^{-1}$ (Hatakeyama et al. 2003)	N.A

Results

With the novel *in silico* model, first we aim to verify our model against 3D migration experiments of human fibroblasts in collagen and fibrin under a specific PDGF-bb gradient (Moreno-Arotzena et al. 2015). Secondly, we observe how different PDGF-bb gradient concentrations regulate cellular 3D migration chemotaxis. At last, we identify the conditions for ECM and factor concentration that promote a more efficient chemotaxis.

During cell migration, we identify three main mechanisms that coordinate cell chemotaxis. First, the cell senses its chemical surroundings in order to probe the chemo-attractant distribution. Then, the cell extends its protrusions and anchors them to the ECM. Finally, when protrusions contract, the cell-ECM interactions determine how the motion will be defined (Fraley et al. 2010).

Based on this observation the proposed model is organized as shown in Figure 4, where we combine the three mechanisms, each one corresponding to a different migration stage. Notably, the proposed model conserves the stochastic aspect chemosensing thus introducing randomness to the predicted results.

Comparison with three-dimensional migration experiments in collagen and fibrin

Given the stochastic nature of the proposed model, for each combination of factor concentration and matrix, we simulated the 3D chemotaxis of ten MSCs for a three hours period. In this first analysis, we compare the model predictions of cell migration trajectories and speeds for cells embedded in collagen and fibrin ECMs, i.e. in similar conditions to those applied *in vitro* by Moreno-Arotzena et al. (2015).

When a cell is surrounded by a chemical gradient (Figure 5(A)) the amount of chemo-attractant surrounding the cell is different in each direction (Figure 5(B)). Accordingly, if a chemo-attractant gradient is established in the 0° direction, i.e. aligned with the cell antero-posterior

Table 3. Mechanical properties of the ECM and filopodia (Zaman et al. 2005; Moreno-Arotzena et al. 2014; Moreno-Arotzena et al. 2015).

	Elasticity (Pa)	Poisson's coefficient	Viscosity (Pa s)
Collagen	39 (Moreno-Arotzena et al. 2015)	0.3	100 (Zaman et al., 1992)
Fibrin	780 (Moreno-Arotzena et al. 2015)	0.3	300 (Moreno-Arotzena et al. 2015)
Protrusion	2×10^9 (Mofrad & Kam 2006; Li et al. 2014)	0	–

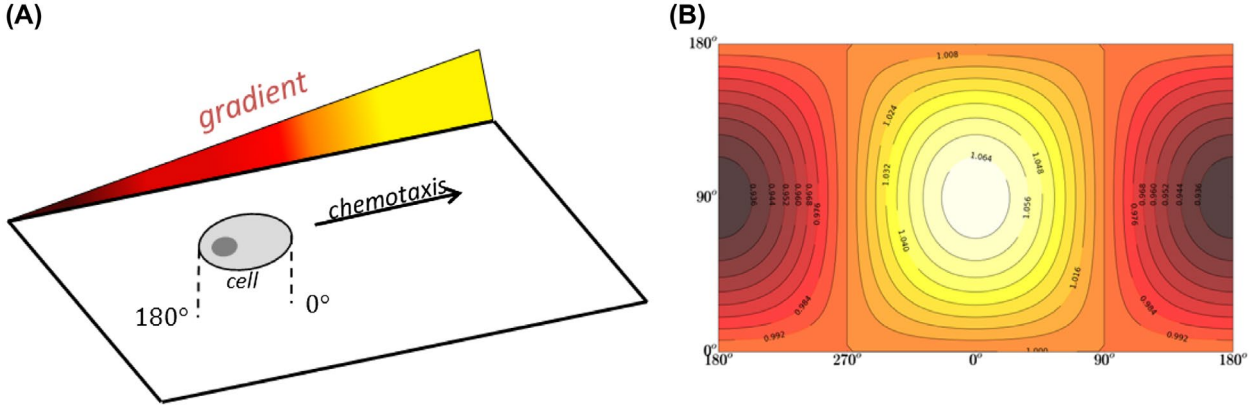

Figure 5. Migration scheme of one cell and factor concentration distribution over its membrane, with a 7% gradient in a 1 ng mL^{-1} concentration, idealizing the cell membrane as the surface of a sphere. Cells have three dimensional membranes and when placed under a gradient such as in situation (A), the factor producing the gradient will have a characteristic distribution across the membrane as shown in (B).

Notes: As a consequence, chemical reactions which coordinate chemosensing will preferentially occur in the membrane surface with higher concentrations. Note that in B we represent the distribution of factor concentration over the membrane surface, thus mapping the spherical data onto a flat surface.

axis, as represented in Figure 5(A), the anterior side of the cell (270°–90°) will face a greater concentration than the rear side of the cell (90°–270°), as illustrated in Figure 5(B).

In fact, the chemosensing pathway starts at the receptor level, as the chemo-attractant will first react with its corresponding membrane receptor. Therefore the chemo-attractant factor activates its receptor more often in the front surface of the cell (270°–90°), i.e. signaling the cell to move towards that direction.

As we can observe from cell trajectories depicted in Figure 6, despite the type of ECM surrounding the cell, we notice that most cells 'advance', reasonably aligned with the gradient direction at 0°. In both ECMs, due to the stochastic nature of the chemotactic signal, which feeds the chemosensing mechanism, cells do not have a straightforward trajectory (Figure 6). Instead, for each haul, cells move in a certain direction at a certain speed, which makes its path irregular. Similarly to what is observed *in vitro* by Moreno-Arotzena et al. (2015), cells draw their trajectory at ±45° around the gradient aligned at 0°. Occasionally, cells turn their backs on the gradient, although in the end, their overall migratory direction tends to be aligned with it. Bearing in mind that cell motion depends on pulling protrusion (motion Equation (12)), we can say that protrusions appearing in the front part of the cell are the ones that tend to pull more frequently, thus leading and regulating the cell movement. Importantly, one can remark right from Figure 6 that cells embedded in a fibrin matrix tend to move less and more slowly than cells in a collagen matrix (see also Supplementary Video 1 and 2).

For cell migration in both collagen and fibrin ECMs, the average speed of fibroblasts is presented in Table 4. We can see how the computed average speeds are very similar to those measured *in vitro* by Moreno-Arotzena et al. (2015). Similarly to what is observed *in vitro,* the average speed ranges within the same order of magnitude, in both collagen and fibrin ECM, although it is clear that cells move more rapidly in collagen.

In fact, cells tend to move faster in collagen as it is a more compliant matrix. Fibrin gels are stiffer and with a higher dynamic viscosity (Moreno-Arotzena et al. 2014), thus impairing dendritic protrusions and cell motility (Table 3).

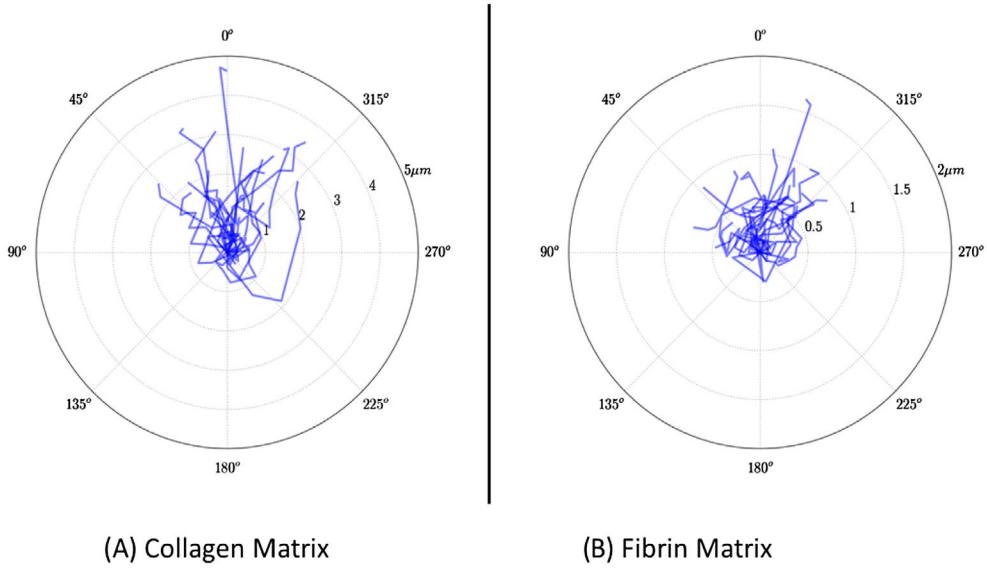

Figure 6. Trajectories observed in (A) collagen and (B) fibrin.
Notes: In both ECMs cells follow the chemical cue provided by the chemical gradient at 0°. Most trajectories are within the ±45° range meaning that they accurately sense the chemo-attractant molecules. However, the effective displacement in fibrin is much lower than in collagen. Note that that the length scale in fibrin is more refined than in collagen.

Table 4. Average cell speed (in μm min^{-1}) in collagen and fibrin ECM.

	Average cell speed in collagen ECM (μm min^{-1})		Average cell speed in fibrin matrix (μm min^{-1})	
PDGF-bb (ng mL^{-1})	*In vitro* (Moreno-Arotzena et al. 2015)	*In silico*	*In vitro* (Moreno-Arotzena et al. 2015)	*In silico*
10^0	0.044	0.048	0.023	0.013
10^1	0.030	0.043	0.025	0.013

Note: For each entry $n = 10$, each *in silico* simulation corresponds to a 3 h migration period *in vitro*.

We also quantitatively predicted the size of the protrusions produced by the cell. As we can see on Table 5, the size predicted by the numerical simulations are within the range obtained *in vitro* by Moreno-Arotzena et al. (2015). As expected, slightly smaller protrusions are grown in fibrin as it is a stiffer matrix. Nonetheless, actin polymerization seems to be strong enough (Table 3) and allows protrusions to pierce through both ECMs although it does so more easily in collagen.

Different gradient concentrations produce a bimodal migrating response

To provide a better understanding on how fibroblasts migrate under a specific chemical factor. We numerically test the migratory response of fibroblasts under the 7% gradient at different chemo-attractant concentrations: 10^{-2}, 10^{-1}, 10^{0}, 10^{1} and 10^{2} ng mL^{-1}, as illustrated in Figure 7.

In Figures 8 and 9, we can observe the polar distribution of the speed vector for each haul, showing directionality, in collagen and fibrin respectively. In agreement with the trajectory results of Figure 6, we note that, for all concentrations, speed vectors align preferentially with the 0°, 45° and 315° directions, indicating that the speed vector direction is biased towards the direction imposed by the gradient.

Bearing in mind that cell motion depends on pulling protrusions (see motion Equation (12)), we can say that protrusions occurring in the anterior side of cells are the ones that tend to pull more frequently. Consequently, these protrusions lead cell motion preferentially in the gradient direction, which causes cell speeds to be more aligned with the gradient. This last observation is illustrated in Figures 8 and 9, where we clearly see that the distribution of cell speed vectors tend to be aligned and gathered around the gradient direction.

In terms of the speed amplitudes reached for the range of concentrations tested, the average and effective speeds are shown in Figure 10. For both cases, the lowest speeds are always obtained for the lowest concentration (1×10^{-2} ng mL^{-1}). From there, cell speed increases as the amount of factor increases. We remark that cell speed peaks around 1×10^{0} ng mL^{-1}. After this peak, cell speed diminishes for even larger concentration of chemoattractant factor (1×10^{1}, 1×10^{2} ng mL^{-1}). This speed distribution is observed for both the cell average speed and the effective speed, which reflects the alignment between speed vector and the cell trajectory.

According to Moreno-Arotzena et al. (2015) higher cell speeds can be obtained for chemo-attractant concentrations as low as 10^{0} ng mL^{-1} and increasing the factor concentration does not always translates into a greater cell speed. In fact, the results obtained *in silico* also suggest this feature as shown in Figures 10 and 11. Again, contrarily to what one might expect, pouring more factor into the cell surroundings does not necessarily imply a greater migration speed.

Therefore, chemotaxis induces a bimodal behavior on 3D cell migration. For low and high concentration of PDGF-bb, low migration speeds are observed, whereas for intermediate concentrations higher migration speeds are attained.

Table 5. Average sizes of protrusions obtained *in vitro* and *in silico*, in both ECMs: collagen and fibrin.

	Collagen matrix		Fibrin matrix	
	In vitro (Moreno-Arotzena et al. 2015)	*In silico*	*In vitro* (Moreno-Arotzena et al. 2015)	*In silico*
Protrusion size (μm)	41–79	41.2	38–78	39.7

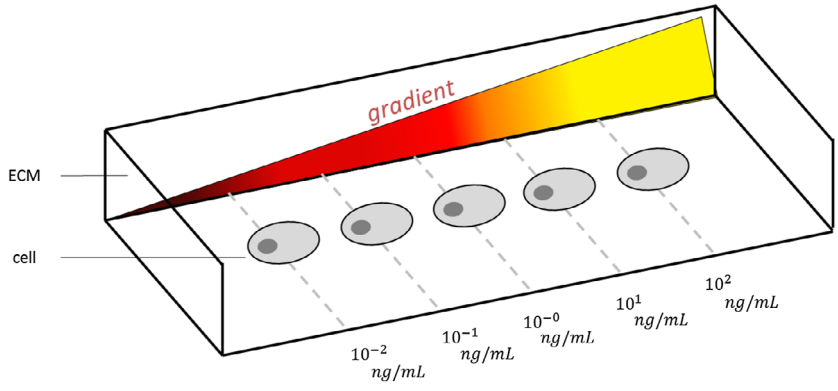

Figure 7. Initial conditions of gradient and surrounding concentrations imposed before the beginning of fibroblast chemotaxis.
Notes: Within the same concentration gradient, different cells are placed at different concentrations levels.

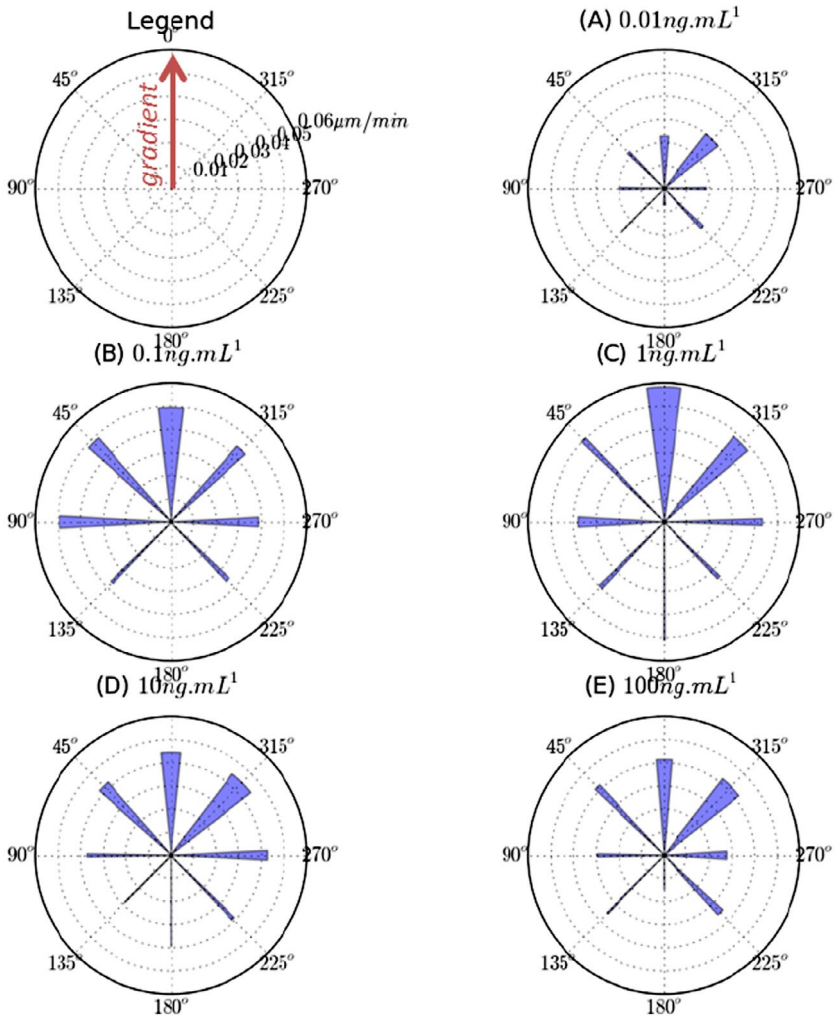

Figure 8. Polar histograms with the orientation of the speed vectors in collagen matrix, for different concentrations of PDGF-bb: (A) 0.01 ng mL^{-1} (B) 0.1 ng mL^{-1} (C) 1 ng mL^{-1} (D) 10 ng mL^{-1} (E) 100 ng mL^{-1}.
Notes: In the polar histograms, each bar stands for the speed vectors that are predicted in one of the 8 main directions ±22.5°; each bar amplitude reflects the average speed of the speed vectors in each direction; the width of each bar reflects the amount of vectors aligned with that direction.

Cell migration efficiency depends on ECM and growth factor concentration

Given the data gather so far, we can try to identify what are the conditions that improve 3D cell migration, for specific cell type, ECM and factor concentration. If we focus first on the role of ECM, we can see the trajectories presented in Figure 6. Actually, a different pattern is found for the trajectories depending on the ECM. So, the trajectories in fibrin form some kind of blob, like a woolen ball, whilst in collagen trajectories picture a more stretched and elongated pattern, which reflects the migration of a larger effective distance. This fact had also been reported by Moreno-Arotzena et al. (2015), and can be quantitatively observed in Figure 10. In fact, cells in both matrices present average speeds within the same order of magnitude, while the effective speeds in collagen are one order of magnitude higher. Basically this reflects the difficulty cells have in transducing their chemosensing into effective cell motion, they can have rapid hauls but overall, it is difficult to leave the initial position. This is illustrated in Table 5, where we show the relative amounts of average and effective speeds that are aligned with the gradient (that we denote by efficiency). As we can see, despite the chemosensing mechanism being independent from the ECM, we clearly notice that cells can more easily align themselves with the gradient when the surrounding ECM is more compliant (collagen). Although the average speed efficiency in fibrin is not that far apart from the average speed efficiency in collagen, this difference accumulates over time and is reflected in the effective speed efficiency (Table 6).

In terms of the amount of factor used, the effect of its concentration is clearly noticed from Figure 10. Although, higher cell speeds are reached for concentration close to 1 ng mL^{-1}, it is clear that even if we use 100 times less factor

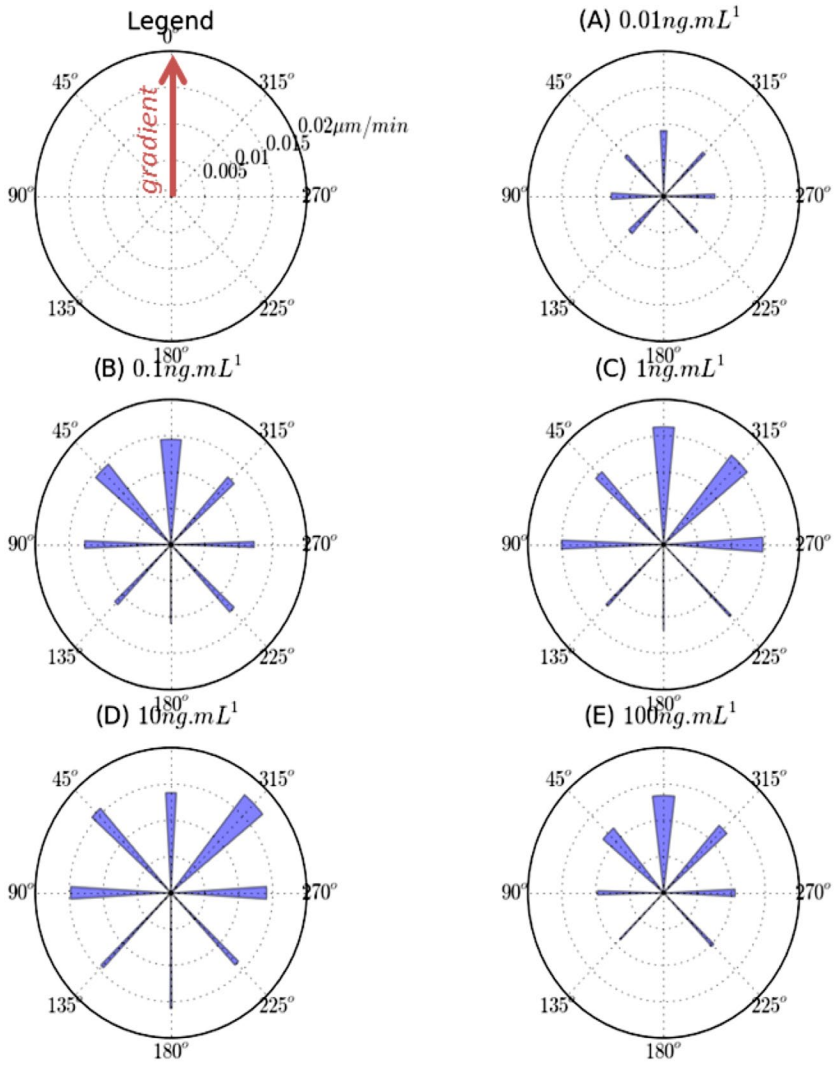

Figure 9. Polar histograms with the orientation of the speed vectors in fibrin matrix, for different concentrations of PDGF-bb: (A) 0.01 ng mL^{-1} (B) 0.1 ng mL^{-1} (C) 1 ng mL^{-1} (D) 10 ng mL^{-1} (E) 100 ng mL^{-1}.

Notes: In the polar histograms, each bar stands for the speed vectors that are caught in one of the 8 main directions ±22.5°; each bar amplitude reflects the average speed of the speed vectors in each direction; the width of each bar reflects the amount of vectors aligned with that direction.

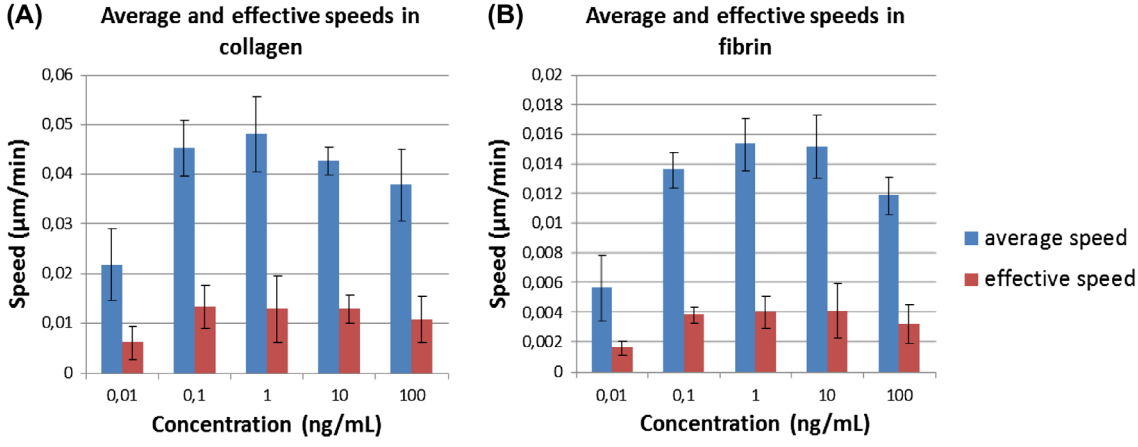

Figure 10. Speeds obtained as function of the concentration in (A) collagen and (B) fibrin. Both histograms (A) and (B), show that the predicted average and effective cell speed is PDGF-bb dependent.

Notes: Cell motility is reduced in fibrin compared to collagen and, in both ECMs, the average and the effective speed distribution is centered around its peak a 1 ng mL^{-1}. For higher and lower concentrations the average and effective speeds are reduced. In a nutshell, the predicted cell speeds are factor concentration dependent and present a bimodal (or *U*-shaped) behavior.

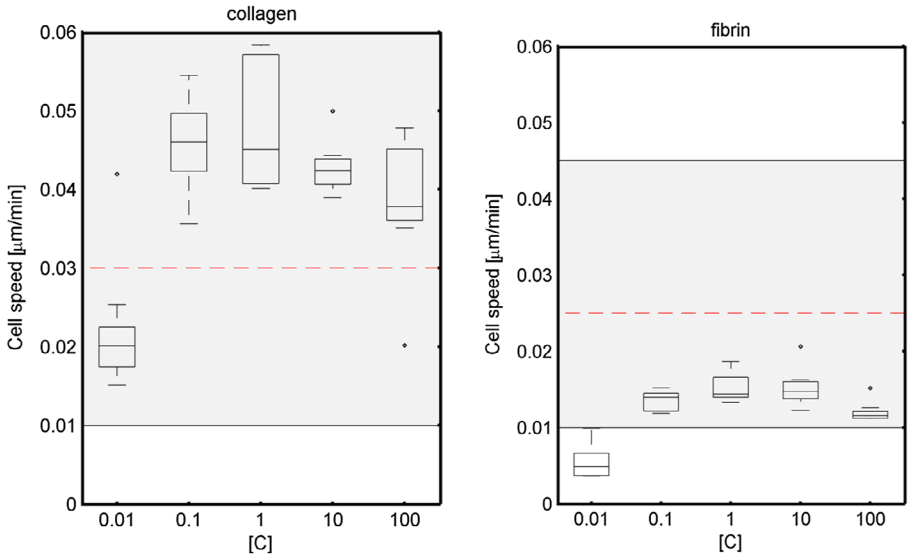

Figure 11. Boxplots that show the median, 25% percentile and 75% percentile of the mean cell speed numerically predicted in the whole chip for collagen (left) and fibrin (right).
Note: Grey area represents the 25–75 percentiles of the experiments and the red discontinuous line its mean value.

Table 6. Average and effective speed efficiency, i.e. their amount that is aligned with the gradient direction. We can notice that systematically, the effective speeds in collagen in collagen are higher than in fibrin, meaning that in collagen, a more compliant ECM, cells can more easily align with the gradient.

	Collagen	Fibrin
Average speed efficiency (%)	44.72	33.16
Effective speed efficiency (%)	78.0	60.5

(0.01 ng mL^{-1}) the cell predicted speeds are still within the same order of magnitude. Therefore, it is more efficient to use lower concentration of chemo-attractant, particularly within the 0.01–1 ng m^{-1}. In particular this would imply that, contrarily to higher concentration, small changes on the amount of factor would lead to greater variations in cell speed, thus allowing a better control over cell migration. As a matter of fact, it is interesting to remark that *in vivo*, the observed range of this type of chemical factor ranges within this interval (Park et al. 2008; Wang et al. 2009, 2011).

Discussion

Mesenchymal chemotaxis migration in 3D is a complex cell process that involves an intricate set of regulatory mechanisms, mediated by multiple micro-environmental cues. Although not comprehensively understood, we assume that three central mechanisms can explain mesenchymal migration: chemosensing, protrusion dynamics and cell-ECM interaction. In this first approach, we simplify this complex process in order to provide a better understanding of the influence of ECM and chemo-attractant concentration on fibroblast 3D chemotactic migration.

In order to validate the proposed model, we first showed that both qualitatively, the presented *in silico* results were in agreement with those obtained *in vitro* by Moreno-Arotzena et al. (2015). Briefly, collagen is a more compliant matrix. Thus, it allows for a better cell movement causing cells to migrate at higher speeds and better aligned with the gradient. Conversely, fibrin is a stiffer matrix, with a tighter filament network that considerably entangles and impairs cell motion. By varying the concentration of the gradient, we found that contrarily to what one might expect, cells do not always move faster in a medium with more factor. Instead a bimodal (*U*-shaped) behavior was observed, where initially an increment in concentration is followed by an increment in cell speed (Lind et al. 1996; Fiedler et al. 2002). After peaking at 10^0 ng mL^{-1}, cells' speed starts decreasing again.

Overall, the effect of ECM and the influence of the amount of chemo-attractant on cell migration patterns were predicted. Nonetheless, despite capturing some important features and patterns of 3D chemotaxis migration, the proposed model is based on some simplifications that should be explained and justified. As a matter of fact, compared to the immense complexity of mesenchymal migration, the model used is reasonably simplified. Yet it considers the fundamental 3D mesenchymal migration mechanisms, thus providing a good predictive capability.

First of all, the complex cascade of chemical reactions that regulates chemosensing was simplified. In fact, although two central elements of the process are taken into account, such as the receptor and the activated PI3K*, the intricate system of cytosolic positive and negative feedbacks (Hatakeyama et al. 2003) is not considered.

However, as shown by Ueda and Shibata (2007), an understanding of the chemosensing can be reached at this early level in the chemosensing pathway, as this work proposes. A more detailed chemical reaction pathway could have been considered, although it would significantly increase the computational time as the Gillespie's algorithm used, slowly but accurately, treats one reaction at the time (Gillespie 1976; Higham 2007). In addition, we evaluate the chemical signal at the base of the protrusion; however, this signal could also be evaluated at its tip. A further analysis will be developed to analyze this effect in future works.

Secondly, the modeling approach taken for cell migration is mostly based on the macroscopic mechanical properties of the surrounding matrix, thus underestimating the local effects due to fibrous architecture of the matrix and matrix fiber (Wang et al. 2014; Escribano et al. 2015; Kim et al. 2015; Mark et al. 2016). The drag generated by the ECM represents the main physical mechanism that controls cell speed, as presented on Equation (10). This simplification definitely limits the coverage of other known effects that help tuning cell drag and speed during MSCs migration (Evan-Ram & Yamada 2005). In fact, other cell-ECM interactions may influence cell migration, i.e. matrix pore size, pore connectivity and matrix fiber. Actually, the consideration of these mechanisms could improve the quantitative predictions between the *in silico* and *in vitro* results.

Finally, in this work we used a simple definition of chemotaxis, i.e. cell migration triggered by a chemical gradient imposed in the extracellular media. Nevertheless, other elements could be involved: e.g. a chemical gradient of molecules embedded in the ECM (haptotaxis (Moreno-Arotzena et al. 2014)), or the cell steepening of the chemical gradient due to directional consumption of factor by the cell itself in order to enhance migration. In future works, these alternative phenomena are going to be considered so as to catch the broader interplay between chemotaxis and haptotaxis, and to provide a deeper understanding on 3D mesenchymal migration.

Disclosure statement

No potential conflict of interest was reported by the authors.

Funding

This work was supported by the European Research Council (ERC) through Project [ERC-2012-StG 306751]; the Spanish Ministry of Economy and Competitiveness [DPI2015-64221-C2-1-R]; Fundação para a Ciência e Tecnologia (FCT), through IDMEC, under LAETA [project number UID/EMS/50022/2013], through the PhD [grant number SFRH/BD/80458/2011].

References

Bear JE, Haugh JM. 2014. Directed migration of mesenchymal cells: where signaling and the cytoskeleton meet. Curr Opin Cell Biol. 30:74–82.

Beauchemin C, Dixit NM, Perelson AS. 2007. Characterizing T cell movement within lymph nodes in the absence of antigen. J Immunol. 178:5505–5512.

Bogle G, Dunbar PR. 2010. Simulating T-cell motility in the lymph node paracortex with packed lattice geometry. Immunol Cell Biol. 88:172–179.

Borau C, Kamm RD, García-Aznar JM. 2011. Mechano-sensing and cell migration: a 3D model approach. Phys Biol. 8:066008.

Campellone KG, Welch MD. 2010. A nucleator arms race: cellular control of actin assembly. Nature Rev Mol Cell Biol. 11:237–251.

Cao RH, Bjorndahl MA, Religa P, Clasper S, Garvin S, Galter D, Meister B, Ikomi F, Tritsaris K, Dissing S. 2004. PDGF-BB induces intratumoral lymphangiogenesis and promotes lymphatic metastasis. Cancer Cell. 6:333–345.

Clyne T, Withers PJ. 1995. An introduction to metal matrixes composites, Cambridge solid state science series. Cambridge University Press: Cambridge.

Condeelis J, Singer RH, Segall JE. 2005. The great escape: when cancer cells hijack the genes for chemotaxis and motility. Annu Rev Cell Dev Biol. 21:695–718.

Cukierman E, Pankov R, Stevens DR, Yamada KM. 2001. Taking cell–matrix adhesion to the third dimension. Science. 294:1708–1712.

Deuel TF, Kawahara RS, Mustoe TA, Pierce GF. 1991. Growth factors and wound healing platelet-derived growth factor as model cytokine. Annu Rev Med. 42:567–584.

Devrotes P, Janetopoulos C. 2003. Eukaryotic chemotaxis: distinctions between directional sensing and polarization. J Biol Chem. 278:20445–20448.

Escribano J, Sánchez MT, García-Aznar JM. 2015. Modeling the formation of the cell–matrix adhesion on a single 3D matrix fiber. J Theor Biol. 384:84–94.

Eshelby J. 1957. The determination of the elastic field of an ellipsoidal inclusion and related problems. R Soc Proc A. 1226:376–396.

Evan-Ram S, Yamada KM. 2005. Cell migration in 3D matrix. Curr Opin Cell Biol. 17:524–532.

Even-Ram S, Doyle AD, Conti MA, Matsumoto K, Adeelstein RS, Yamada KM. 2007. Myosin IIA regulates cell motility and cactomyosin-microtubule crosstalk. Nat Cell Biol. 9:299–309.

Fiedler J, Röderer G, Günther KP. 2002. BMP-2, BMP-4, and PDGF-bb stimulate chemotactic migration of primary human mesenchymal progenitor cells. J Cell Biochem. 87:305–312.

Fraley SI, Feng Y, Krishnamurthy R, Kim D, Celedon A, Longmore GD, Wirtz D. 2010. A distinctive role for focal adhesion proteins in three-dimensional cell motility. Nat Cell Biol. 12:598–604.

Friedl P, Wolf K. 2009. Plasticity of cell migration: a multiscale tuning model. J Cell Biol. 188:11–19.

Friedl P, Wolf K. 2010. Plasticity of cell migration: a multiscale tuning model. J Cell Biol. 188:11–19.

Geris L, Gerisch A, Sloten JV, Weiner R, Oosterwyck HV. 2008. Angiogenesis in bone fracture healing: A bioregulatory model. J Theor Biol. 251:137–158.
Gillespie DT. 1976. A general method for numerically simulating the stochastic time evolution of coupled chemical reactions. J Comp Phys. 22:403–434.
Giri A, Bajpai S, Trenton N, Jayatilaka H, Longmore GD, Wirtz D. 2013. The Arp2/3 complex mediates multigeneration dendritic protrusions for efficient 3-dimensional cancer cell migration. FASEB J. 27:4089–4099.
Hatakeyama M, Kimura S, Naka T, Kawasaki T, Yumoto N, Ichikawa M, Kim JH, Saito K, Saeki M, Shirouzu M, Yokoyama S, Konagaya A. 2003. A computational model on the modulation of mitogen-activated protein kinase (MAPK) and Akt pathways in heregulin-induced ErbB signaling. Biochem J. 373:451–463.
Hawkins PT, Anderson KE, Davidson K, Stephens LR. 2006. Signalling through class I PI3Ks in mammalian cells. Biochem Soc Trans. 34:647–662.
Heinecke K, Seher A, Werner S, Mueller TD, Sebald W, Nickel J. 2009. Receptor oligomerization and beyond: a case study in bone morphogenetic proteins. BMC Biol. 7:59–79.
Higazi AA, Kniss D, Manuppello J, Barnathan ES, Cines DB. 1996. Thermotaxis of human trophoblastic cells. Placenta. 17:683–687.
Higham D. 2007. Modeling and simulating chemical reactions. SIAM Rev. 50:347–368.
Insall RH. 2010. Understanding eukaryotic chemotaxis: a pseudopod-centered view. Nat Rev Mol Cell Biol. 11:453–458.
Jilkine A, Edelstein-Keshet L. 2011. A comparison of mathematical models for polarization of single eukaryotic cells in response to guided cues. Plos Comput Biol. 7:e1001121.
Kim MC, Neal DM, Kamm RD, Asada HH. 2013. Dynamic modeling of cell migration and spreading behaviors on fibronectin coated planar substrates and micropatterned geometries. PloS Comput Biol. 9:e1002926.
Kim MC, Whisler J, Silberberg YR, Kamm RD, Asada HH. 2015. Cell invasion dynamics into a three dimensional extracellular matrix fibre network. Plos Comput Biol. 11:e1004535.
Lämmermann T, Bader BL, Monkey SJ, Worbs T, Wedlich-Soldner R, Hirsch K, Keller M, Froster R, Critchley DR, Fässier R. 2008. Rapid leukocyte migration by integrin-independent flowing and squeezing. Nature. 453:51–55.
Lebensohn AM, Kirschner MW. 2009. Activation of the WAVE complex by coincident signals controls actin assembly. Mol Cell. 36:512–524.
Li T, Gu YT, Oloyede A, Yarlagadda PK. 2014. Molecular investigation of the mechanical properties of single actin filaments based on vibration analyses. Comput Methods Biomech Biomed Eng. 17:616–622.
Lind M, Eriksen EF, Bünger C. 1996. BMP-2 but not BMP-4 and -6 stimulates chemotactic migration of human osteoblasts, human marow osteoblasts, and U2-OS cells. Bone. 18:53–57.
Liou Y, Tong W, Kao Y, Sung K, Lee C, Kuo P. 2014. Substrate stiffness regulates filopodial activities in lung cancer cells. Plos One. 9:e89767.
Lo CM, Wang HB, Dembo M, Wang YL. 2000. Cell movement is guided by the rigidity of the substrate. Biophys J. 79:144–152.
Mark M, Spill F, Kamm RD, Zaman MH. 2016. Single-cell migration in complex microenvironments: mechanics and signaling dynamics. J Biomech Eng. 138:021004-1–021004-8.
Martin P, Parkhurst SM. 2004. Parallels between tissue repair and embryo morphogenesis. Development. 131:3021–3034.
Miller AF, Harvey SA, Thies RS, Olson MS. 2000. Bone morphogenetic protein-9. An autocrinte/paracrine cytokine in the liver. J Biol Chem. 275:17937–17945.
Mofrad MRK, Kam RD. 2006. Cytoskeletal mechanics, model and measurements in cell mechanics. Cambridge University Press: Cambridge.
Moreno-Arotzena O, Borau C, Movilla N, Vicente-Manzanares M, García-Aznar JM. 2015. Fibroblast migration in 3D is controlled by haptotaxis in a non-muscle myosin II-dependent manner. Ann Biomed Eng. 43:3025–3039.
Moreno-Arotzena O, Meier JG, del Amo C, García-Aznar JM. 2015. Characterization of fibrin and collagen gels for engineering wound healing models. Materials. 8:1636–1651.
Moreno-Arotzena O, Mendoza G, Cóndor M, Rüberg T, García-Aznar JM. 2014. Inducing chemotactic and haptotactic cues in microfluidic devices for three-dimensional *in vitro* assays. Biomicrofluidics. 8:064122.
Paralkar VM, Weeks BS, Yu YM, Kleinman HK, Reddi AH. 1992. Recombinant human bone morphogenetic protein 2B stimulates PC12 cell differentiation: potentiation and binding to type IV collagen. J Cell Biol. 119:1721–1728.
Park Y, Kim JW, Kim DS, Kim EB, Park SJ, Choi WS, Song JG, Seo HY, Oh SC, et al. 2008. The bone morphogenesis protein-2 (BMP-2) is associated with progression to metastatic disease in gastric cancer. Cancer Res Treat. 40:127–132.
Pelletier DB, Boyten AL. 1994. Dissociation of PDGF receptor tyrosine kinase activity from PDGF-mediated inhibition of gap junctional communication. J Cell Physiol. 158:427–434.
Petri PJ, Doyle AD, Yamada KM. 2009. Random versus directionally persistent cell migration. Nat Rev Mol Cell Biol. 10:538–549.
Poukkula M, Cliffe A, Changede R, Rørth P. 2011. Cell behaviors regulated by guidance cues in collective migration of border cells. J Cell Biol. 192:513–524.
Rangarajan R, Zaman ZH. 2008. Modeling cell migration in 3D. Cell Adh Mig. 2:106–109.
Roca-Cusachs P, Sunyer R, Trepat X. 2013. Mechanical guidance of cell migration: lessons from chemotaxis. Curr Opin Cell Biol. 25:543–549.
Rotty JD, Wu C, Bear JE. 2013. New insights into the regulation and cellular functions of the ARP2/3 complex. Nat Rev Mol Cell Biol. 14:7–12.
Saltzman E, Drew JH, Leemis LM, Henderson SG. 2012. Simulating multivariate nonhomogeneous Poisson process using projections (Article 15). ACM Trans Model Comput Simul. 22:1–13.
Shaw TJ, Martin P. 2009. Wound repair at glance. J Cell Sci. 122:3203–3208.
Starke J, Maaser K, Wehrle-Haller B, Friedl P. 2013. Mechanotransduction of mesenchymal melanoma cell invasion into 3D collagen lattices: filopod-mediated extension-relaxation cycles and force anisotropy. Exp Cell Res. 319:2424–2433.
Swaney KF, Huang CH, Devreotes PN. 2010. Eukaryotic chemotaxis: a network of signaling pathways controls motility, directional sensing, and polarity. Annu Rev Biophys. 39:265–289.

Ueda M, Shibata T. 2007. Stochastic signal processing and transduction in chemotactic response of eukaryotic cells. Biophys J. 93:11–20.

Valero C, Javierre E, Garcia-Aznar JM, Gómez-Benito MJ. 2014. A cell-regulatory mechanism nivolving feedback between contraction and tissue formation guides wound healing progression. Plos One. 9:e92774.

Veevers-Lowe J, Ball SG, Shuttleworth A, Kielty CM. 2011. Mesenchymal stem cell migration is regulated by fibronectin through alpha5beta1-integrin-mediated activation of PDGFR-beta and potentiation of growth factor signals. J Cell Sci. 124:1288–1300.

Vicente-Manzanares M, Newell-Litwa K, Bachir AI, Whitmore LA, Horwitz AR. 2011. Myosin IIA/IIB restrict adhesive and protrusive signaling to generate front-back polarity in migrating cells. J Cell Biol. 14:196–202.

Wang C, Yang KD, Ko J, Huang C, Huang H, Wang F. 2009. The effects of shockwave on bone healing and systemic concentrations of nitric oxide (NO), TGF-β1, VEGF and BMP-2 in long bone non-unions. Nitric Oxide. 20:298–303.

Wang H, Abhilash AS, Chen CS, Wells RG, Shenoy VB. 2014. Long-range force transmission in fibrous matrices enabled by tension-driven alignment of fibers. Biophys J. 107:2592–2603.

Wang YK, Sun WF, Liu XG, Deng J, Yan BE, Jiang WY, Lin XB. 2011. Comparative study of serum level of BMP-2 and heterotopic ossification in traumatic brain injury and fracture patients. Zhongguo Gu Shang. 24:399–403.

Weiger MC, Ahmed S, Welf ES, Haugh JM. 2010. Directional persistence of cell migration coincides with stability of asymmetric intracellular signaling. Biophys J. 98:67–75.

Zaman MH, Kamm RD, Matsudaira P, Lauffenburger DA. 2005. Computational model for cell migration in three-dimensional matrices. Biophys J. 89:1389–1397.

Appendix

The value of the parameters used in all the simulations were estimated by means of quantitative comparisons with the experimental results from Moreno-Arotzena et al. (2015):

Parameter	Description
$s_{new\_protrusion} = 20$ **(adimensional)**	Signal threshold for protrusion birth
$s_{growth} = 10$ **(adimensional)**	Signal threshold for protrusion growth
$s_{ret} = 10$ **(adimensional)**	Signal threshold for protrusion death
$a_{growth} = 0.1$ mm and $\beta_{growth} = 25$ **(adimensional)**	Parameters used to determine length increment based on PI3K* signal
$a_{ret} = 0.07$ mm and $\beta_{ret} = 25$ **(adimensional)**	Parameters used to determine length increment based on PI3K* signal
$a_{adh} = 5 \times 10^{-4}$ N mm^{-1}	Coefficient relating protrusion length with traction force